

C00000147

RADIATION TRANSPORT FROM THE BOTTOM OF THE REACTOR CORE TO THE BOTTOM OF THE REACTOR PRESSURE VESSEL OF THE PBMR

Oscar M. Zamonsky/ PBMR (Proprietary)
Limited. Lake Buena Vista Building. Centurion.
RSA.

ABSTRACT

This paper describes the methodology used to perform the transport of neutrons from the bottom of the reactor core up to a surface below the reactor pressure vessel of the PBMR. The calculations were done with the MCNP code. A fairly detailed analysis of the Weight Windows used as variance reduction for the MCNP calculations is presented as well as a sensitivity analysis about different ways to construct fixed sources for the MCNP code.

INTRODUCTION

This paper presents the calculations performed to transport neutrons from a known fixed neutron source at a surface located at the bottom of the defuelling cones up to a surface located at the shielding floor below the Reactor Pressure Vessel (RPV) of the PBMR.

The calculations were performed with the MCNP code [1].

The system where the transport was done (Figures 1, 2 and 3) is divided into three parts, according to the intrinsic characteristics of each part that affects the transport of neutrons. The region above the bottom plate of the core barrel, Figures 1 and 2, is composed of internal components of the core barrel, the RPV and gaps between the RPV and the citadel wall (CW). The core barrel (steel) contains the bottom reflector (graphite), the defuel chutes (fuel spheres) and large helium transporting components that form the core outlet pipe (COP). The region between the bottom plate of the core barrel and the shielding floor of the RPV, Figure 3, contains the RPV (steel) and the defuel chutes. The shielding floor of the RPV is composed of Heavy Concrete.

The heterogeneities, the slowing down caused by the large graphite region (6 meters high approximately) and the absorptions in iron and in heavy concrete hamper the accurate transport of neutrons, mainly at fast energies. Therefore, some variance reduction techniques such as source biasing, weight windows and splitting/Russian roulette were applied to solve the transport problem. This paper in particular gives a fairly detailed analysis of the weight windows used to solve the transport problem.

Two external source definitions were used as input to the MCNP calculations. One external source is simply defined by reading a source file written by a previous MCNP run, and the other is defined by constructing a fixed source from an MCNP output.

The first definition is more accurate than the second one since the written source files contain all the information of the particles that form the source. However, one of the advantages of using a constructed fixed source is that it allows for flexibility in solving the problem. In particular, it makes it possible to use parallel processors, which is not currently possible with our version of the MCNP code.

This paper presents a sensitivity analysis for these two ways of defining the fixed sources for the MCNP calculations.

GEOMETRY MODEL

This Section describes the geometry model used to perform the transport of neutrons with the MCNP code.

Figure 1 shows the geometry, as represented in MCNP, above the bottom plate of the Core Barrel inside the RPV, while Figure 2 shows the same region but extended up to the Citadel Wall. The different colors in the bottom reflector represent different temperatures of the Graphite. The fuel spheres inside the defuel chutes (DC), as well as the kernels inside the pebbles, are modelled explicitly

Figure 3 shows the geometry modelled below the bottom plate of the core barrel. The details of the RPV dome and the shielding floor below the RPV are evident in this figure.

In the description of the geometry, the origin of coordinates is located at the intersection of the core centre line and the Core Outlet Pipe (COP) centre line. The axial z coordinate increases from bottom to top and the x coordinate increases from left to right, see Figure 1.

Note that the bottom reflector contains several material discontinuities given by the interfaces between graphite and helium, Figure 1. These channels, plenums and pipes together with the gaps shown in Figure 2 are important neutron streaming routes. Figure 4 shows an X-Y section of the system modeled corresponding to the axial level $z = 0$ cm.

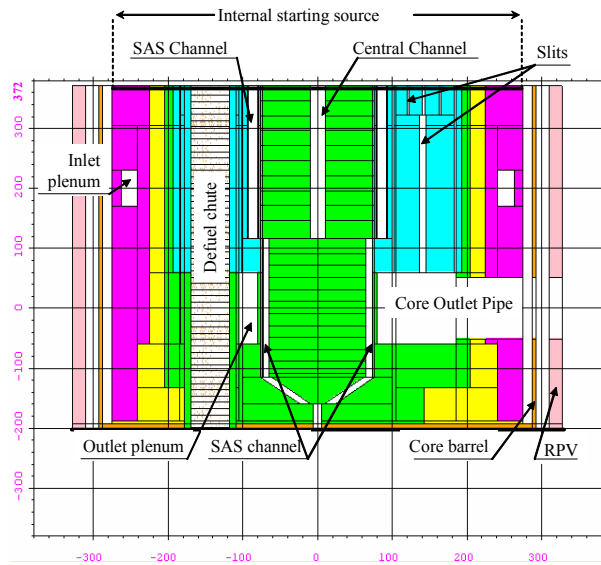


Figure 1. X-Z section of the MCNP model for the 1TIS

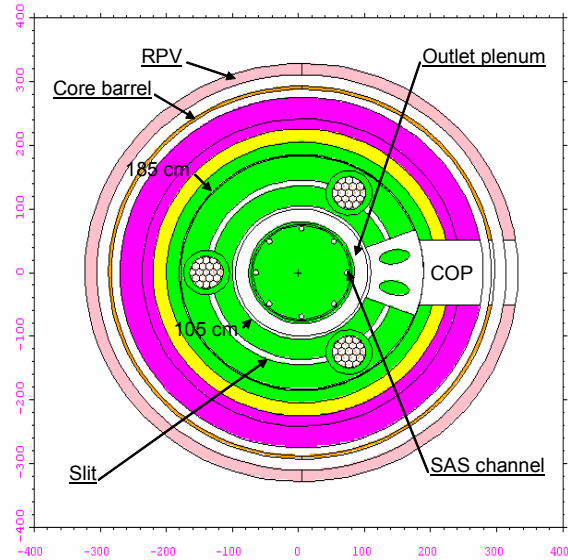


Figure 4. X-Y section of the MCNP model at $z = 0$ cm

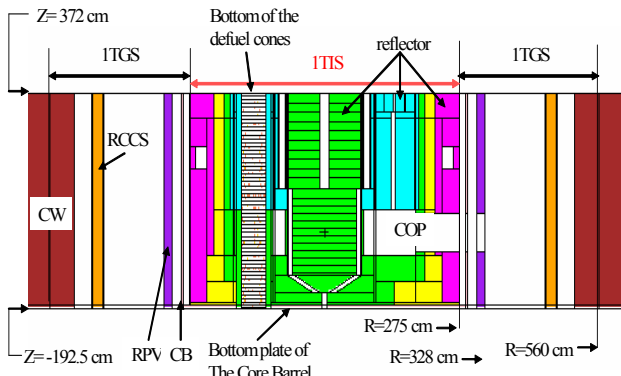


Figure 2. X-Z section of the MCNP model for the 1TGS

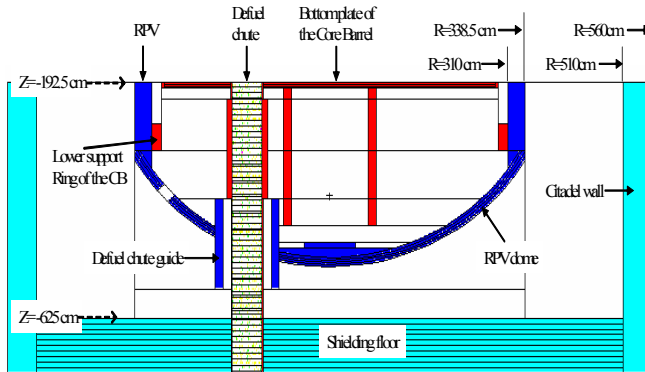


Figure 3. X-Z section of the MCNP model for the second transport

METHODOLOGY

The downward neutron current at the shielding floor below the RPV, $z = -645$ cm, was calculated starting from the downward neutron current obtained from the model reported in [2] at the bottom of the defueling cones, $z = 372$ cm, for the reactor core operating at a power of 400 MWth. This transport also takes into account neutrons coming from fissions in the fuel inside the defuel chutes.

The calculations were performed in the following steps:

- 1TIS: First Transport with Internal Starting Source (ISS):** This is the calculation of the downward neutron current in a surface at the top of the bottom plate of the Core Barrel, $z = -192.5$ cm, starting from the source at $z = 372$ cm inside the region $r < 275$ cm provided by [2]. This starting source does not extend to any gap of the system since it ends at the outer surface of the reflector, $r = 275$ cm. The system for which the calculations were done is contained inside the region $-205.5 < z < 372$ cm and $r < 328$ cm, i.e. it extends axially from the bottom of the defueling cones to the upper surface of the bottom plate of the Core Barrel, inside the outer surface of the RPV, $r = 328$ cm. The system modeled for the 1TIS is detailed in Figure 1.
- 1TGS: First Transport with Source at the Gaps (GSS):** This is the calculation of the downward neutron current at $z = -192.5$ cm, starting from the source at $z = 372$ cm within the region $275 < r < 560$ cm, [2]. This source extends through the gaps between the outer surface of the reflector and the Citadel Wall. The system for which the calculations were done contains the system modelled for the 1TIS but ranges up to $r = 860$ cm, i.e., it includes the Citadel Wall. The system modelled for the 1TGS is detailed in Figure 2
- 2TIS: Second Transport corresponding to the First Transport with Internal Source:** This refers to the calculation of the downward neutron current at $z = -645$ cm starting from the information of the neutrons

crossing surface $z = -192.5$ cm in downward directions obtained with the 1TIS calculations. The system modelled for this transport is inside the region $-725 < z < -192$ cm and $r < 560$ cm, i.e. it ranges from the top of the bottom plate of the core barrel to a surface inside the shielding floor below the RPV, and includes 50 cm of the citadel wall. The system modelled for the 2TIS is shown in Figure 3.

- **2TGS: Second Transport corresponding to the First Transport with Source at the Gaps:** This refers to the calculation of the downward neutron current at $z = -645$ cm starting from the information of the neutrons crossing surface $z = -192.5$ cm in downward directions obtained with the 1TGS calculations.

SOURCE MODELLING

The fixed surface neutron source used for the first transport, cases 1TIS and 1TGS, was prepared from the downward neutron current calculated according to the model given in [2] at the bottom of the reactor core, $z = 372$ cm. This was a criticality calculation of the reactor core done with the MCNP code for a power of 400 MWth.

The radial discretization used to tally this current in the criticality calculation is detailed in Table 1, the angular discretization is shown in Table 2 and the energy discretization corresponds to the XMAS 172 Group Energy Structure [3]. Note that the polar angles in Table 2 are measured relative to the vector $(0,0,-1)$.

Let $\psi(\vec{r}, \hat{\Omega}, E)$ be the angular flux at position \vec{r} , direction $\hat{\Omega}$ and energy E . Then, the partial current given by the criticality calculation, j_{igm} , is

$$j_{igm} \equiv \int_{A_i} d^2\vec{r} \int_{\Delta E_g} dE \int_{\Delta \hat{\Omega}_m} d\hat{\Omega} |\hat{\Omega} \cdot \hat{n}| \psi(\vec{r}, \hat{\Omega}, E) \quad (1)$$

where the surfaces A_i correspond to the annulus contained within the radius given in Table 1, the solid angle limits for the intervals $\Delta \hat{\Omega}_m$ are shown in Table 2 and the energy limits for the intervals ΔE_g are the XMAS 172 groups.

Table 1. Radial discretization for the starting source

From [cm]	To [cm]	Description
0.0	10.0	Central channel
10.0	76.0	Central reflector
76.0	100.0	Central reflector
100.0	109.0	Below core
109.0	135.0	Below core
135.0	150.0	Below core
150.0	176.0	Below core
176.0	185.0	Below core
185.0	225.0	Inner side reflector

From [cm]	To [cm]	Description
225.0	275.0	Outer side reflector
275.0	287.5	Gap reflector - Core Barrel
287.5	292.5	Core Barrel
292.5	310.0	Gap Core Barrel - RPV
310.0	328.0	RPV
328.0	448.96	Gap RPV – RCCS
448.96	451.15	RCCS inner steel wall
451.15	473.45	RCCS water
473.45	475.64	RCCS outer steel wall
475.64	510.0	Gap RCCS – citadel wall
510.0	560.0	Citadel wall (50 cm inside)

Table 2. Angular discretization for the starting source.

Angular boundaries [degrees]						
0 - 5	5 - 10	10 - 20	20 - 30	30 - 45	45 - 60	60 - 90

From the downward current j_{igm} , an incoming fixed source was evaluated and included as an external surface source in the model described in this paper (*starting source*).

The starting source was spatially divided into two disjoint sources: one inside region $r < 275$ cm that does not include any gap, and another inside the region $275 < r < 560$ cm (i.e. ranging from the outer side reflector to 50 cm inside the citadel wall).

The first source was used in the system shown in Figure 1, i.e. a system contained inside the pressure vessel, case 1TIS. The second source was applied to the system shown in Figure 2, which contains the previous system and extends up to the citadel wall, case 1TGS.

Since both systems were solved using disjoint sources, the total downward current at $z = -192.5$ cm is equal to the sum of the downward currents obtained in each system.

Note that the division of the first transport in cases 1TIS and 1TGS can be considered as correct if the partial currents at $z = -192.5$ cm and $r > 275$ cm obtained from 1TIS are negligible compared to those obtained from 1TGS. This assumption was verified with the results obtained.

Both previously described sources were determined from the criticality calculation using the same approach, which is explained in the following paragraphs.

The space, angle and energy discretization used to define the starting source is the same as the one tallied in the criticality calculation, i.e. Table 1, Table 2 and XMAS 172 groups respectively, and it is assumed that every spatial sector has the same angular and energy dependence.

Being S_{igm} the starting source for region i , energy group g and angular interval m , it was evaluated as:

$$S_{igm} = \frac{\sum_{g'm'} j_{ig'm'}}{\sum_{i'g'm'} j_{i'g'm'}} \sum_{i'} j_{i'gm} \quad (2)$$

In Eq. 2, the sums over energy and angle extend over all energy and angle intervals tallied in the criticality calculation, while the sums over the spatial index extend over the intervals of the criticality calculation that are contained in each source interval. For example, for the case corresponding to the 1TIS, the sums over the first index go from the first to the tenth interval of Table 1, and they range from the eleventh to the last interval of Table 2, in the 1TGS case.

Note that in Eq. 2, $\sum_{i'} j_{i'gm}$ accounts for the energy and angle dependence of the source, hence, it is assumed that the same energy and angle dependence applies to all the space regions in which the source was discretized.

The spatial dependence of the source was taken into account by the relative intensities of the source inside a given sector and the total source in the problem to be solved,

$$\frac{\sum_{g'm'} j_{ig'm'}}{\sum_{i'g'm'} j_{i'g'm'}} \quad \text{in Eq. 2.}$$

The previous approximations were done since the card provided in MCNP to model a fixed source (SDEF) allows only one level of dependency in the definition of the fixed source. This level was used for the angle and energy dependence of the source, and the spatial dependence was given as another bin.

Following the previously described procedure, the spectra shown in Figures 5, 6 and 7 denoted as “source” were obtained for each region. In these figures, the spectra denoted as “tallied” correspond to the downward currents obtained in the criticality calculation.

The tallied intensity for the region that contains the defuel chutes, $100 < r < 185$ cm, is 55% of the total intensity tallied in region $0 < r < 275$ cm. Therefore, it is expected that the spectrum tallied in this region dominates the spectrum of the constructed source as confirmed in Figure 6.

Figure 5 shows that for the central column, which contributes 30% of the total source intensity, the spectrum of the fixed source obtained is harder than the corresponding tallied spectra. The same effect can be observed in Figure 7 for the external region, which represents 15% of the total source intensity.

These approximations together with the homogenization of the defuel chutes in the region contained within $100 < r < 185$ cm could affect the accuracy of the results obtained in the first transport. A sensitivity analysis for the procedure used to construct the fixed surface source is performed in Annex A. From this analysis it is possible to conclude that the approximations made to construct the starting source detailed in this section are accurate enough to obtain acceptable results for the first transport.

The fixed sources used for the second transport, cases 2TIS and 2TGS, are read from written surface source files of cases 1TIS and 1TGS.

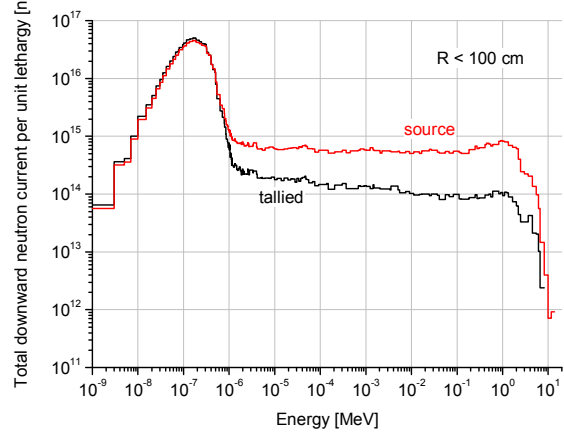


Figure 5. Tallyed and constructed fixed source spectra per unit lethargy for $z = 372$ cm and $R < 100$ cm.

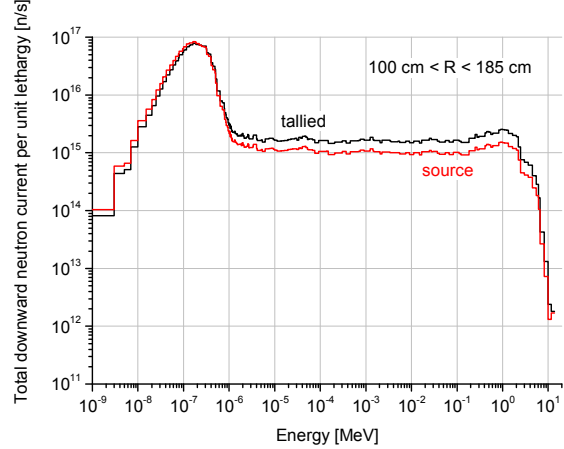


Figure 6. Tallyed and constructed fixed source spectra per unit lethargy for $z = 372$ cm and $100 < R < 185$ cm.

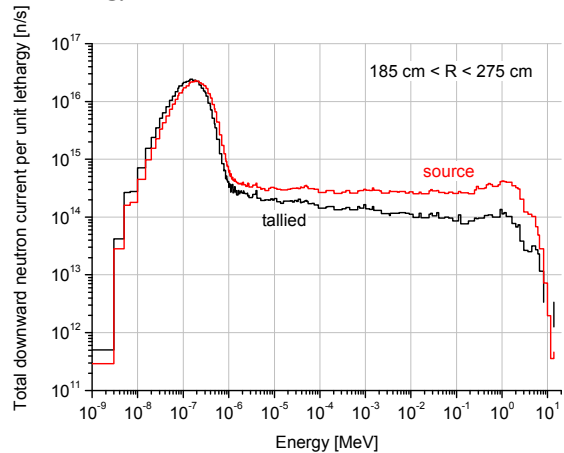


Figure 7. Tallyed and constructed fixed source spectra per unit lethargy for $z = 372$ cm and $185 < R < 275$ cm.

FIRST TRANSPORT

The first transport denotes the MCNP calculations performed for the system shown in Figures 1 and 2. The starting source for the first transport was constructed from downward currents obtained in a criticality calculation of the reactor core applying the methodology described in the previous Section. The first transport was performed in two disjoint calculations, cases 1TIS and 1TGS.

The information of neutrons crossing the upper surface of the bottom plate of the Core Barrel in downward directions was written in an external file. This file was used as starting source for the second transport, cases 2TIS and 2TGS.

The variance reduction techniques used to perform the transport of neutrons for the 1TIS were source biasing and weight windows. For the 1TGS only source biasing was used.

Source biasing was done in three energy groups with upper limits equal to 0.625 eV, 1.0 MeV and 20.0 MeV.

Weight windows were generated using the mesh-based weight windows generator of the MCNP code. They were generated at two energy groups with upper limits equal to 0.625 eV and 20.0 MeV. The procedure used to estimate the weight windows for the 1TIS is detailed in Annex B.

Figure 8 shows the radial shape of the downward neutron current obtained with models 1TIS and 1TGS at $z = -192.5$ cm. Note that from the outer surface of the bottom reflector ($r = 275$ cm) to the outer surface of the RPV, the contribution to the downward neutron current from the 1TGS is higher than the contribution from the 1TIS. This observation supports the approximation done in the geometry model used in the 1TIS case where the system ranges up to $r = 328$ cm.

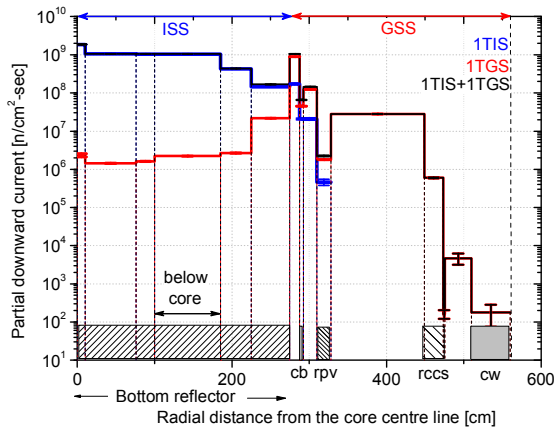


Figure 8. Radial distribution of the downward neutron current at $z = -192.5$ cm

Figure 9 shows the downward neutron current spectra per unit lethargy at $z = -192.5$ cm, calculated in the first transport cases 1TIS plus 1TGS and integrated inside four annular regions that cover the entire system. It is interesting to note the shape of the current for fast energies in the annulus $100 < r < 185$ cm where the fission spectra becomes evident.

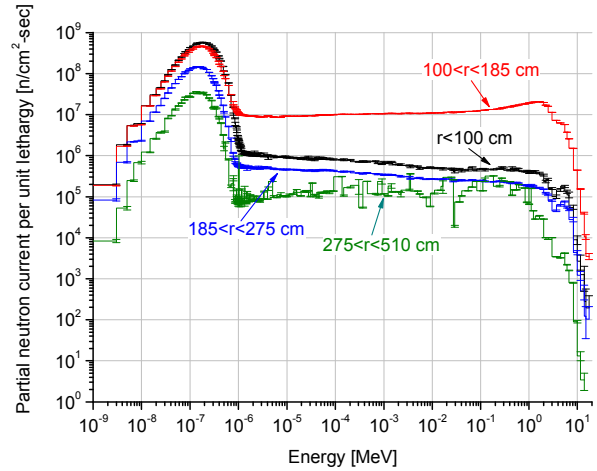


Figure 9. Downward neutron current spectra per unit lethargy obtained from the first transport calculation at $z = -192.5$ cm (1TIS+1TGS)

Figure 10 and Figure 11 show the logarithmic R-Z contour plot of the fast ($E > 0.1$ MeV) and thermal ($E < 3$ eV) neutron scalar flux in the bottom reflector obtained in the first transport, 1TIS+1TGS. The fluxes plotted are averaged over 2π . It is interesting to note the propagation of the fast flux through void regions such as the centre cooling channel, the outlet plenum and core outlet pipe, Figure 10, and the high thermal flux in almost the entire reflector, Figure 11.

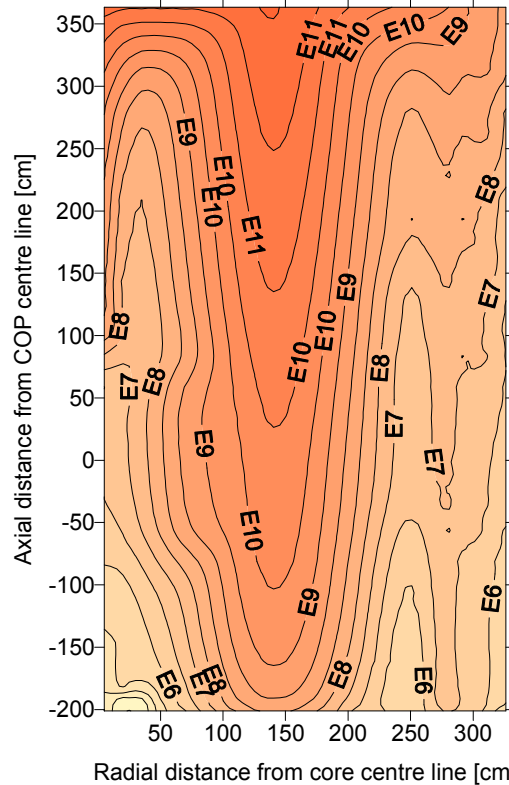


Figure 10. Logarithmic R-Z contour plot of the fast scalar neutron flux ($E > 0.1$ MeV) in the bottom reflector

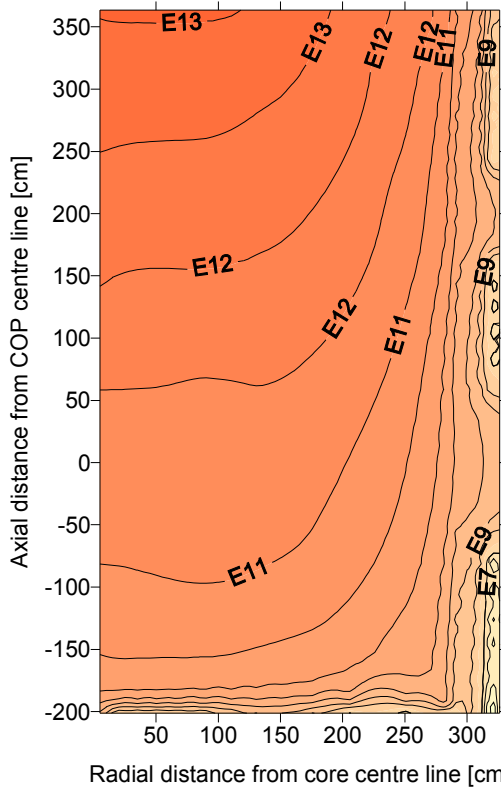


Figure 11. Logarithmic R-Z contour plot of the thermal scalar neutron flux ($E < 3$ eV) in the bottom reflector

Some low discretized downward neutron currents were calculated at $z = -192.5$ cm in order to have control on the convergence of the MCNP runs. They were evaluated inside the four annular regions shown in Figure 12 and within three energy groups of upper limits equal to 0.625 eV, 1.0 MeV and 20.0 MeV. The convergence checks and the statistical indicators provided by the MCNP runs leads us to the conclusion that the results shown in this paper are correct.

SECOND TRANSPORT

The second transport denotes the MCNP calculations performed for the system shown in Figure 3. The starting source for the second transport is the source file written at $z = -192.5$ cm from the solutions of cases 1TIS and 1TGS.

The second transport was performed in two disjoint calculations, cases 2TIS and 2TGS. These cases read disjoint sources coming from cases 1TIS and 1TGS respectively - refer to Figure 3.

The information of neutrons crossing the surface $z = -645$ cm located inside the shielding floor of the RPV is written in external files. These files should be read as starting sources to perform radiation transport below the shielding floor of the RPV.

The variance reduction technique used in the second transport is splitting/Russian roulette.

Figure 12 shows the downward neutron current spectra per unit lethargy inside four annuli obtained from the second transport calculations (2TIS+2TGS) at the surface $z = -645$ cm. Note that even in the annulus that contains the defuel chutes the fission spectrum is no longer notorious.

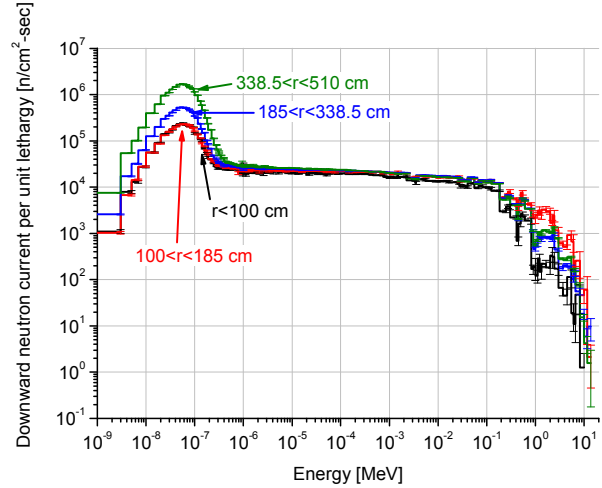


Figure 12. Downward neutron current spectra per unit lethargy obtained from the second transport calculation at $z = -645$ cm (2TIS+2TGS)

A sensitivity analysis of the use of different starting sources is presented in Annex A for the second transport.

The second transport with internal source, case 2TIS, was also solved using a constructed fixed source as starting point. This source was constructed following the same procedure as used for the 1TIS case. The problem solved with this synthetic source will be called 2TIS* in this paper.

Figure 13 shows the same calculated spectra as shown in Figure 12 for the 2TIS case and the ratios of the calculated spectra from case 2TIS* over those obtained with the 2TIS case. It can be seen that this ratio is not greater than 2 for energies lower than 0.1 MeV where the partial currents are better converged. A sensitivity analysis of the use of different starting sources is presented in Annex A for the second transport.

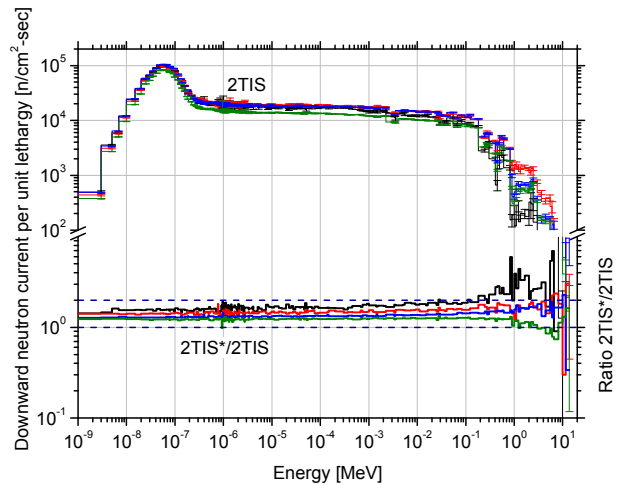


Figure 13. Downward neutron current per unit lethargy at $z = -645$ cm obtained in cases 2TIS and 2TIS*

The same low discretized downward neutron currents calculated for the first transport to have control on the convergence of the MCNP runs were evaluated at $z = -645$ cm. The MCNP checks and statistical indicators provided for the second transport gives us confidence in the results obtained.

CONCLUSIONS

An MCNP model was created to transport neutrons from the bottom of the reactor core to the bottom of the reactor pressure vessel of the PBMR.

The components of the bottom reflector and the bottom part of the RPV were modelled in detail. The fuel inside the defuel chutes was specifically taken into account.

The transport calculation was performed with an external source at the bottom of the defuel cones for the reactor core operating at a power of 400 MWth and taking into account the fissions inside the defuel chutes.

Some variance reduction techniques were applied. They were necessary to improve the sampling of the system and to increase the efficiency of the calculations. The figure of merit of the MCNP calculations, in particular, was increased up to two orders of magnitude using these techniques.

The scalar flux distribution inside the bottom reflector, as well as downward neutron currents at the bottom plate of the core barrel and below the reactor pressure vessel, was calculated. This could also be used to calculate activation and damage of the components and dose rates below the shielding floor of the RPV.

The accuracy of the results was checked following the convergence of statistical parameters provided by the MCNP runs. Further simplified calculations, possibly using deterministic methods, should be done in order to validate the results presented in this paper.

The methodology presented in this paper can be used with minor modifications to perform new transport calculations below the reactor core. In particular, the weight windows for the first transport can be applied even if some modifications are done in the geometry since they were generated in an optimized space and energy discretization.

ACKNOWLEDGMENTS

The author would like to thank PBMR for their financial support and permission to publish this work.

REFERENCES

- [1] X-5 Monte Carlo Team, 1987, "MCNP – A General Monte Carlo N-Particle Transport Code, Version 5". Los Alamos National Laboratory, Report LA-UR-03-1987.
- [2] Albornoz, F. and Korochinsky, S., 2006, "MCNP Modelling of the PBMR Equilibrium Core," Accepted to be presented in the "ANS Topical Meeting on Reactor Physics – PHYSOR 2006", Vancouver, Canada, September 10-14 2006.
- [3] Forrest, R. A. and Gilbert, M. R., 2005, FISPACT-2005 User Manual, EURATOM/UKAEA Fusion Association, Culham Science Centre, Abingdon, Oxfordshire OX14 3DB, UK..

ANNEX A

SENSITIVITY ANALYSIS FOR THE FIXED SOURCE CONSTRUCTION

This Annex presents the analysis of the sensibility of the energy, angle and spatial approximations made to construct the fixed source for the 1TIS.

The analysis is performed by constructing a fixed source for the case 2TIS with the same procedure used to construct the fixed source for case 1TIS. The problem solved with this constructed starting source is called 2TIS* in this paper.

Some results obtained with the constructed source for the second transport, case 2TIS*, are compared with the results obtained by reading the source file written by case 1TIS (i.e. the results of case 2TIS). Therefore, it is assumed that the *reference* results are those obtained for problem 2TIS, since the starting source in this case accounts for all the space-phase variables of all the particles that cross surface $z = -192.5$ cm in all the recorded downward directions.

The solutions analyzed in this section correspond to the downward current tallied inside the annular sectors given in Table 3 within energy limits $E < 0.625$ eV (thermal), $0.625 \text{ eV} < E < 1.0$ MeV (epithermal) and $1.0 < E < 20.0$ MeV (fast).

Table 3. Region boundaries for tallies

From [cm]	To [cm]	Description
0.0	100.0	Internal sector
100.0	185.0	Contains the defuel chutes
185.0	338.5	Up to the external surface of the RPV
338.5	510.0	Up to the internal surface of the citadel wall

The comparative results between the problems solved are shown in Table 4 and the approximations used to obtain them are described below.

In Table 4, the column titled **2TIS** shows the results obtained when reading the written source file for the **1TIS** case. These results are referred to as *reference results* in this paper (problem 2TIS). The other columns show the results for each problem solved as well as the ratio between these results and the reference results, depicted as “*ratio*”.

Column **2TIS*** in Table 4 shows the results obtained for case 2TIS*. It can be seen that these results are higher than the reference results for every energy group. To understand the causes of these differences, the following paragraphs analyze the energy, angle and space treatment used to construct the fixed source for problem 2TIS*.

Energy analysis

The differences in behaviour between the tallied and the constructed spectrum of the downward current tallied at $z = -192.5$ cm is conceptually the same as for the starting source at $z = 372$ cm, Figures 5, 6 and 7. At $z = -172.5$ cm it is also observed that the maximum total downward current is inside the annulus that contains the defuel chutes, $100 \text{ cm} < R < 185$ cm, and, in this region, both the written

source file and the constructed one have very similar behaviours.

In order to analyze the sensitivity of the source with the spectrum, problem **2Teg1** was solved with the fixed source only inside this region and with the same spectra as used for this region in problem **2TIS***. The corresponding results given in Table 4 are less than the reference solutions, except for the fast flux. The ratios of results of **2Teg1** to those of **2TIS*** are between 0.5 and 0.6. This is consistent with the ratio of intensities of the source in both problems, which is equal to 0.53. The results of **2Teg1** are then only useful to have confidence in the way the source was made, but it is not possible to draw any conclusions about the sensitivity of the results with the energy approximation used to construct the fixed source.

The problem denoted as **2Teg2** has the source only inside the region that contains the defuel chutes (as **2Teg1**), but with the spectra corresponding to this region (**2Teg1** has the average spectra used in **2TIS***). Comparing the results of **2Teg2** with those of **2Teg1** it follows that the spectra used in the defuel chutes region affects the results. However, the comparison with the reference results shows that the solutions obtained with **2Teg2** are greater than the reference solutions. It is then possible to conclude that it is not only the spectra used to construct the source that affects the accuracy of the results.

An angular as well as a spatial analysis to determine which approximation has more influence on the results obtained with the constructed source, is presented below.

Angular analysis

The starting source for problem **2TIS*** was constructed in four angular bins with limits of 0° , 15° , 30° , 60° and 90° . By reading the written source file obtained in the first transport, a more detailed angular discretization was tallied for the downward current that was used to construct a new starting source.

Figure 14 shows the approximated angular fluxes obtained from both downward currents for the region $100 \text{ cm} < r < 185$ cm; one with the four bins for which the source of case 2TIS* was constructed and the other with an angular mesh of 5° width between 0° and 90° (zero degrees corresponds to the vector $(0,0,-1)$). The approximated angular fluxes shown in Figure 14 were obtained assuming that the flux is isotropic in the surface where the current was tallied.

The case **2Tang** was solved using the fine angular mesh source constructed inside the region $100 < r < 185$ cm. The spectra used for this fixed source is the same as that used for problem **2Teg2**. Table 4 shows that there are no important differences between the results obtained with problem **2Tang** and those obtained with **2Teg2**. Therefore, it is possible to conclude that the angular discretization is not a very

important parameter to take into account in order to improve the accuracy of the results reached in the 2TIS* case.

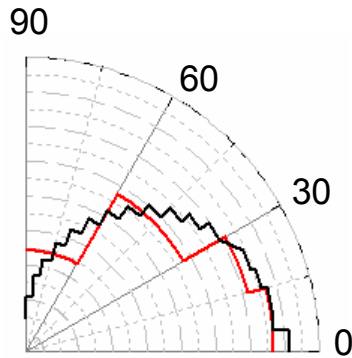


Figure 14. Angular fluxes at $z = -192.5$ cm integrated in the region $100 \text{ cm} < r < 185 \text{ cm}$

Spatial distribution analysis

The third approach analyzed is the spatial discretization used to construct the fixed source for problem 2TIS*. Two problems were solved for this:

- **2Tsp1** where the fixed source is contained only inside the three defuel chutes, and
- **2Tsp2** with the fixed source inside the annular region $100 < r < 185$ cm but excluding the three defuel chutes.

The spectrum of each of the previous cases are those obtained with the 1TIS inside the corresponding region.

The results obtained are given in Table 4 where the column denoted as 2Tsp1+2Tsp2 shows the sum of the results of both problems, i.e. the results for the region $100 < r < 185$ cm with a space discretization that explicitly considers the defuel chutes. The ratios of these solutions to the reference solutions are close to one. Therefore, it can be concluded that this spatial approximation is the most important one regarding the accuracy of the results obtained with the constructed fixed source.

It is important to note that a similar analysis could be done for the starting source used in the first transport. However, it is possible to assume that for the first transport the accuracy of the synthetic source is higher than for the second transport. This assumption can be justified considering that the reactor core is next to the surface where the partial currents were calculated (the bottom of the defuel cones), so the spatial distribution of currents is expected to be much flatter than in the case discussed above.

Table 4. Downward currents at z = -192.5 cm for sensitivity analysis.

	2TIS		2TIS*		2Teg1		2Teg2		2Tang		2Tsp1		2Tsp2		2Tsp1+2Tsp2	
	n/sec	n/sec	ratio	n/sec	ratio	n/sec	ratio	n/sec	ratio	n/sec	n/sec	n/sec	n/sec	n/sec	ratio	
0 to 100 cm																
th	7.12E+09	1.08E+10	1.51	5.88E+09	0.83	9.87E+09	1.39	1.01E+10	1.42	4.48E+09	3.28E+09	7.76E+09	1.09			
epi	6.10E+09	1.01E+10	1.66	5.49E+09	0.90	9.28E+09	1.52	9.42E+09	1.55	3.85E+09	3.00E+09	6.85E+09	1.12			
fast	9.85E+06	2.45E+07	2.49	1.15E+07	1.17	2.30E+07	2.33	3.04E+07	3.08	3.25E+06	6.49E+06	9.74E+06	0.99			
total	1.32E+10	2.09E+10	1.58	1.14E+10	0.86	1.92E+10	1.45	1.96E+10	1.48	8.33E+09	6.28E+09	1.46E+10	1.10			
100 to 185 cm																
th	1.67E+10	2.25E+10	1.35	1.33E+10	0.79	2.23E+10	1.33	2.26E+10	1.35	1.03E+10	7.35E+09	1.77E+10	1.06			
epi	1.67E+10	2.45E+10	1.47	1.44E+10	0.86	2.43E+10	1.45	2.47E+10	1.48	1.03E+10	7.80E+09	1.81E+10	1.08			
fast	1.37E+08	2.09E+08	1.52	1.37E+08	1.00	2.17E+08	1.58	2.37E+08	1.73	7.04E+07	6.79E+07	1.38E+08	1.01			
total	3.36E+10	4.72E+10	1.41	2.78E+10	0.83	4.68E+10	1.39	4.76E+10	1.42	2.07E+10	1.52E+10	3.59E+10	1.07			
185 to 338.5 cm																
th	5.81E+10	7.44E+10	1.28	4.48E+10	0.77	7.34E+10	1.26	7.49E+10	1.29	3.76E+10	2.40E+10	6.17E+10	1.06			
epi	5.45E+10	7.27E+10	1.33	4.41E+10	0.81	7.31E+10	1.34	7.45E+10	1.37	3.48E+10	2.33E+10	5.80E+10	1.07			
fast	1.86E+08	3.23E+08	1.74	1.93E+08	1.04	3.64E+08	1.96	3.68E+08	1.98	8.66E+07	9.75E+07	1.84E+08	0.99			
total	1.13E+11	1.47E+11	1.31	8.90E+10	0.79	1.47E+11	1.30	1.50E+11	1.33	7.24E+10	4.74E+10	1.20E+11	1.06			
338.5 to 510 cm																
th	8.29E+10	1.00E+11	1.21	6.08E+10	0.73	9.93E+10	1.20	1.01E+11	1.22	5.44E+10	3.21E+10	8.65E+10	1.04			
epi	7.15E+10	8.79E+10	1.23	5.39E+10	0.75	8.82E+10	1.23	9.00E+10	1.26	4.66E+10	2.76E+10	7.42E+10	1.04			
fast	3.09E+08	3.58E+08	1.16	2.13E+08	0.69	3.44E+08	1.11	3.69E+08	1.19	1.46E+08	1.01E+08	2.47E+08	0.80			
total	1.55E+11	1.89E+11	1.22	1.15E+11	0.74	1.88E+11	1.21	1.92E+11	1.24	1.01E+11	5.98E+10	1.61E+11	1.04			

ANNEX B

WEIGHT WINDOWS GENERATION FOR THE FIRST TRANSPORT

Fast and epithermal neutrons are difficult to transport from the starting source to the top of the bottom plate of the Core Barrel due to the large region of graphite they have to pass through - refer to Figure 1. Therefore, it is necessary to apply some variance reduction technique to ensure that the system is well-sampled with these neutrons and to increase the efficiency of the calculation.

One of the techniques used in this model is weight windows. Weight windows were generated using the mesh-based weight windows generator of the MCNP code for two energy groups - the thermal one with energies lower than 0.625 eV, and the epithermal and fast group, with energies inside the interval $0.625 \text{ eV} < E < 20 \text{ MeV}$. The target space region used to calculate the importances is the top surface of the bottom plate of the Core Barrel, $z = -192.5 \text{ cm}$ inside the region $r < 275 \text{ cm}$.

To define the energy limits of the weight windows, the relative contribution of both fast neutrons, $E > 1.0 \text{ MeV}$, coming from the top of the system and fast neutrons coming from fissions in the defuel chutes to the neutron current inside the spatial region described above, was analyzed. The results presented below show that fast neutrons coming from fissions in the defuel chutes have a higher contribution to the tallied region than those transported from the starting source. Therefore, it was concluded that the energy discretization of the variance reduction technique can be relaxed and hence applied, not to neutrons with $E > 1.0 \text{ MeV}$, but to those with energies greater than 0.625 eV. This analysis is presented in the following paragraphs.

The axial shape of the average scalar flux was calculated with MCNP for the system inside the regions $0 < r < 100 \text{ cm}$, $100 < r < 185 \text{ cm}$ and $185 < r < 292.5 \text{ cm}$, which will be denoted in this Annex as regions r1, r2 and r3, respectively. Note that region r2 contains the defuel chutes.

Figure 15 shows the axial profile of the scalar flux integrated in the energy range $1.0 < E < 20.0 \text{ MeV}$ for each region, r1, r2 and r3, when fissions in the defuel chutes are taken into account. From these results it follows that the fast flux in region r2 is almost two orders of magnitude higher than the fast flux averaged in regions r1 and r3, when fissions are considered in the defuel chutes.

On the other hand, Figure 16 shows the axial profiles of the scalar flux inside region r2 with and without fissions inside the defuel chutes. From this figure it follows that fissions in this region cause the average flux to be around two orders of magnitude higher than when fissions are not included.

Therefore, it is possible to conclude *a priori* that in region r2, where the scalar flux is higher, the most important contribution to the fast flux comes from fissions rather than from the fast neutrons born in the starting source at the top of the system. In other words, it is expected that the main contribution to the fast neutron current at the bottom plate of the core barrel comes from fissions in the defuel chutes.

Therefore, the energy discretization of fast and epithermal neutrons was relaxed and the weight windows were generated without paying special attention to the transport of fast neutrons from the starting source. Weight windows were then generated for fast and epithermal neutrons together, i.e. they were optimized for energies ranging from 0.625 eV to 20.0 MeV.

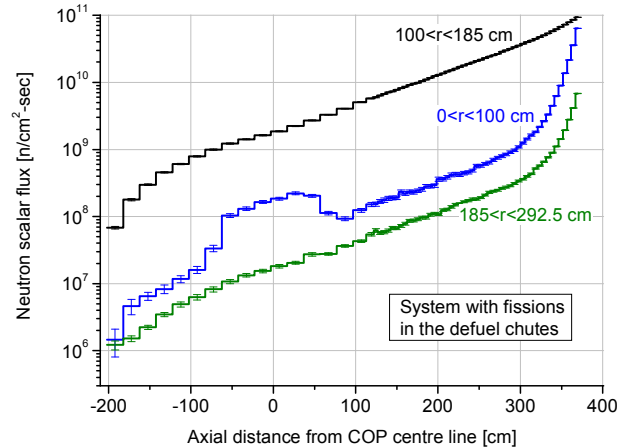


Figure 15. Axial shape of the fast flux, $1.0 < E < 20.0 \text{ MeV}$, for the system with fissions in the defuel chutes

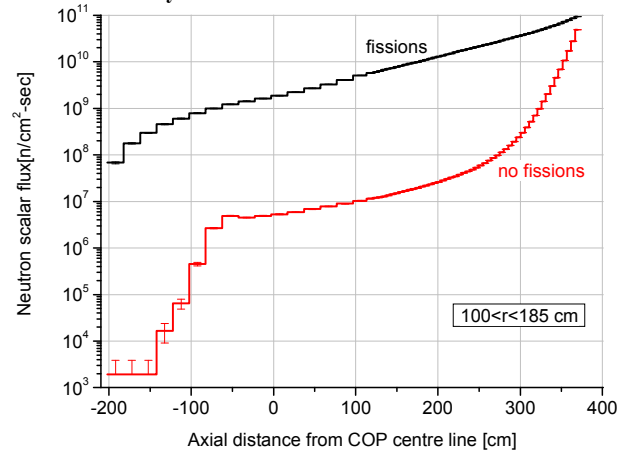


Figure 16. Axial shape of the fast flux inside region r2 for the system with and without fissions in the defuel chutes